Riv. Mat. Univ. Parma, Vol. 2 (2011), 77-98

R. GRZHIBOVSKIS and S. RJASANOW

New applications of the Adaptive Cross Approximation in mechanical engineering

Abstract. Three new applications of the Adaptive Cross Approximation will be reviewed. The first one is devoted to the reconstruction of the three-dimensional metal sheet surfaces obtained via incremental forming techniques by the use of the radial basis functions. In the second application, a calculation of effective elastic moduli in three-dimensional linear elasticity for highly anisotropic composite material is considered. The third application is a coupling of the Finite and Boundary Element Methods for elastic-plastic deformations arising in deep rolling processes.

Keywords. Adaptive Cross Approximation, radial basis functions, incremental metal forming, composite materials.

Mathematics Subject Classification (2000): 65N38, 65N30, 74B05, 74C05, 74E30.

1 - Introduction

The Adaptive Cross Approximation (ACA) was first introduced in [**6**], [**9**] in mathematical and in [**17**] in engineering literature. Now it is a well established technique for approximation of dense matrices of different origin. The main applications lie, however, still by three-dimensional Boundary Element Methods (BEM). In the last years a significant progress has been achieved in both theoretical foundation of the ACA [**8**], [**7**] and in the practical use of this technique in engineering and industry [**18**]. We refer also to the monograph [**21**], where a number of detailed

Received: March 11, 2010; accepted in revised form: January 18, 2011.
This research was partially supported by German Research Foundation, Grant RJ 2/11-3.

academic and more complicated numerical examples are presented. A search string "Adaptive Cross Approximation" in Google gives in March 2010 more than 64 000 matches.

In this article, after a brief description of the ACA in Section 2, we consider three recent ACA applications to three very different problems from mechanical engineering. In Section 3, a smooth reconstruction of three-dimensional metal sheet surfaces obtained via incremental forming techniques with the help of radial basis functions [**4**] is considered. A calculation of effective elastic moduli for highly anisotropic composite materials [**1**] and a coupled FEM/BEM approach for elastic-plastic deformations arising in deep rolling processes [**2**] are based on the ACA accelerated BEM solver. These applications are presented in Section 4.

2 - Adaptive Cross Approximation

When using BEM for the numerical solution of boundary value problems for three-dimensional second order partial differential equations, one has to deal with matrices which are dense, i.e. all their entries do not vanish in general, leading to an asymptotically quadratic memory requirement for the whole procedure. Thus, classical boundary element realisations are applicable only for a rather moderate number N of boundary elements. Fortunately, all boundary element matrices can be decomposed into a hierarchical system of blocks which can be approximated by the use of low rank matrices. This approximation can be computed by the use of the ACA algorithm.

A typical element of a Galerkin-BEM matrix $A \in \mathbb{R}^{N\times M}$ is of the form

$$a_{k,\ell} = \int_\Gamma \int_\Gamma K(x,y)\psi_k(x)\varphi_\ell(y)\,ds_y\,ds_x\,, \quad k = 1,\dots,N\,,\ \ell = 1,\dots,M\,, \tag{1}$$

where $K : \mathbb{R}^3 \times \mathbb{R}^3 \to \mathbb{R}$ is either the fundamental solution of the underlying differential operator or one of its derivatives. The trial functions φ_ℓ as well as the test functions ψ_k are usually with compact support. Let us denote the centers of these supports by

$$X = \{x_k\}_{k=1}^N \quad \text{and} \quad Y = \{y_\ell\}_{\ell=1}^M\,.$$

If the kernel K is smooth then the singular values of the matrix A are exponentially decaying and the matrix can be approximated by a low rank matrix $\tilde{A}$ as follows

$$\|A - \tilde{A}\|_F \le \varepsilon\|A\|_F\,, \quad \operatorname{rank}\tilde{A} = r(\varepsilon)\,,$$

where the rank $r = r(\varepsilon)$ is a logarithmic function of the required accuracy but does

not depend on the dimensions N and M. Therefore, a linear memory requirement for the matrix $\tilde{A}$ is achieved

$$Mem(\tilde{A}) = \mathcal{O}\big(r(\varepsilon)(M+N)\big)\,.$$

The best possible approximation in any unitary invariant norm is given due to the Mirsky theorem [**20**] by the truncated Singular Value Decomposition (SVD) of the original matrix A. In BEM, however, the kernel function, as we already have mentioned above, is the fundamental solution of a differential operator, and, therefore, exposes an algebraic singularity for $x \to y$ and is infinitely smooth for $x \neq y$. Such functions are asymptotically smooth, i.e. it holds

$$\big|\partial_x^\alpha \partial_y^\beta K(x,y)\big| \leq c_p\, p!\, |x-y|^{-p} \big|K(x,y)\big|\,, \quad \text{for all } \alpha,\beta \in \mathbb{N}_0^3\,, \tag{2}$$

where $p = |\alpha+\beta|$. For asymptotically smooth functions, the admissibility condition

$$\min\big\{\operatorname{diam} X\,,\, \operatorname{diam} Y\big\} \leq \eta \operatorname{dist}(X,Y)\,, \quad 0<\eta<1 \tag{3}$$

guarantees existence of a degenerate approximation

$$K(x,y) \approx \tilde{K}(x,y) = \sum_{k=1}^{r(\varepsilon)} u_k(x)\, v_k(y)\,, \quad \text{for all } x \in X\,,\ y \in Y\,,$$

where the rank $r = r(\varepsilon)$ depends only on the required accuracy ε. Thus, the Galerkin matrix (1) constructed on an admissible pair (X, Y) will be of the low rank $r(\varepsilon)$ independent of its dimension. However, the original sets X and Y are, of course, not admissible. The usual way to obtain an approximation is an hierarchical decomposition of the matrix in a system of blocks which corresponds to an hierarchical decomposition of the sets X and Y in two systems of clusters and determination of the admissible cluster pairs corresponding to the condition (3). Instead of going into details, we refer to the monograph [**21**] and demonstrate a hierarchical decomposition of an approximation of the surface of the unit sphere with $N = M = 1280$ plane triangles in a system of clusters on Figure 1 as well as an admissible cluster pair on Figure 2. The final matrix is then so called hierarchical matrix [**14**] and we illustrate its structure in Figure 3, where the quadratic matrix of the single layer potential is shown on the left and the rectangular double layer potential matrix is depicted on the right. In practice, the optimal approximation of the single blocks of a hierarchical matrix can not be computed with SVD due to its high computational costs. The ACA algorithm instead delivers a good quality approximation in almost linear complexity. In this paper, we present a version of the ACA, so called "Fully pivoted ACA" which is also not asymptotically optimal but very clear and easy to understand. Let $A \in \mathbb{R}^{N\times M}$ be a block of a hierarchical matrix.

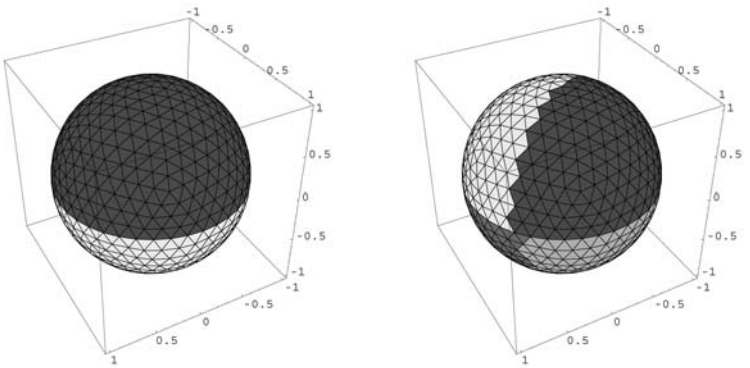

Fig. 1. Clusters of the level 1 and 2 for $N = 1280$.

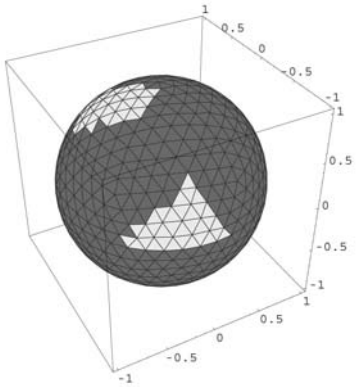

Fig. 2. An admissible cluster pair for $N = 1280$.

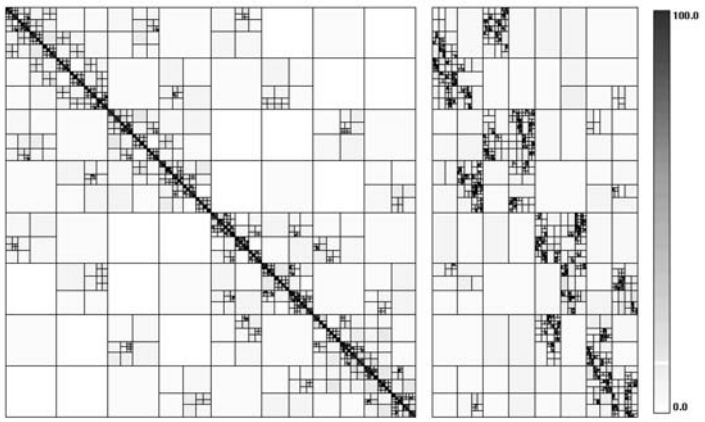

Fig. 3. Partitioning of the BEM matrices for $N = 5120$ and $M = 2562$.

Algorithm 2.1.

1. *Initialisation*

$$R_0 = A\,,\ S_0 = 0\,.$$

2. *For* $i = 0, 1, 2, \ldots$ *compute*

2.1. *pivot element*

$$(k_{i+1}, \ell_{i+1}) = \quad \mathrm{ArgMax}|(R_i)_{k\ell}|\,,$$

2.2. *normalising constant*

$$\gamma_{i+1} = \left((R_i)_{k_{i+1}\ell_{i+1}}\right)^{-1},$$

2.3. *new vectors*

$$u_{i+1} = \gamma_{i+1} R_i e_{\ell_{i+1}}\,,\ v_{i+1} = R_i^{\top} e_{k_{i+1}},$$

2.4. *new residual*

$$R_{i+1} = R_i - u_{i+1} v_{i+1}^{\top}\,,$$

2.5. *new approximation*

$$S_{i+1} = S_i + u_{i+1} v_{i+1}^{\top}\,.$$

In Algorithm 2.1, e_j denotes the jth column of the identity matrix I. The whole residual matrix R_i is inspected in Step 2.1 of Algorithm 2.1 for its maximal entry. Thus, its Frobenius norm can easily be computed in this step, and the appropriate stopping criterion for a given $\varepsilon > 0$ at step r would be

$$\|R_r\|_F \le \varepsilon \|A\|_F\,.$$

We refer again to [**21**] for more complicated but asymptotically optimal partially pivoted ACA algorithm.

3 - Interpolation with radial basis functions

Radial basis functions (RBFs) have become increasingly popular for the construction of smooth interpolant $s : \mathbb{R}^n \to \mathbb{R}$ through a set of N scattered, pairwise distinct data points $(x_i, f_i)_{i=1}^N$, $x_i \in \mathbb{R}^n$ (see [**15, 10, 5, 13, 11**]). The interpolant is introduced as

$$s(x) = \sum_{i=1}^{N} a_i \phi(|x - x_i|) + P_m(x), \tag{4}$$

where a_i are unknown coefficients, P_m is an mth-degree polynomial, and ϕ is a basis function. In addition to the interpolation condition $s(x_k) = f_k$ at each data point, we require

$$\sum_{k=1}^{N} a_k q_j(x_k) = 0$$

for each basis function $q_j(x)$, $j = 1, \ldots, l(m)$, in the $l(m)$-dimensional space of mth-degree polynomials in $\mathbb{R}^n$. This yields a system of linear algebraic equations,

$$\begin{pmatrix} \Phi & Q \\ Q^\top & 0 \end{pmatrix} \begin{pmatrix} a \\ c \end{pmatrix} = \begin{pmatrix} f \\ 0 \end{pmatrix}, \tag{5}$$

where $\Phi_{ij} = \phi(|x_j - x_i|)$, f is the vector of data values f_i, a is the vector containing the unknown coefficients a_i, c is the vector of coefficients of P_m with respect to the basis $(q_k)_{k=1}^{l(m)}$, and $Q_{ij} = q_j(x_i)$. The system has a unique solution if ϕ is strictly conditionally positive-definite of order $m + 1$ and the set of data points is unisolvent for the space of polynomials of degree m [**19**]. This procedure does not require an underlying mesh and produces an accurate, differentiable interpolant.

In our application, the data comes from optical measurements of sheet metal parts. The top and the bottom surfaces of the part are measured in a fixed frame of reference, and a distribution of thickness along the part is sought. We, therefore, restrict ourselves to data in $\mathbb{R}^2$, i.e. $x_i = (x_{i,1}, x_{i,2})$, and make use of the thin plate spline (TPS) basis function

$$\phi(r) = r^2 \log(r) \tag{6}$$

which is conditionally positive-definite of order two. Thus, a first-degree polynomial,

$$P_1(x) = c_1 + ((c_2, c_3)^\top, x)$$

must be inserted into (4) to guarantee the invertibility of system (5).

The form of (6) implies, that the matrix Φ is fully populated. It is easy to check, however, that the function (6) satisfies (2) i.e. is asymptotically smooth. Therefore, the matrix Φ can be efficiently approximated by a blockwise low-rank (hierarchical) matrix as shown in Section 2. The approximant can then be utilised to solve the system (5) by means of GMRES iterative procedure [**22**]. In these settings the whole interpolation procedure has almost linear complexity and almost linear storage requirement. Because of the large condition number of the system matrix in (5) the quality of the blockwise low-rank approximation has to be high. In our computations the value of the ACA epsilon was set to 10^{-10}.

The performance of the resulting interpolation procedure on synthetic data sets is summarized in Table 1. The memory requirement ("*Mem*") is given along with the

Table 1. *Performance of the interpolation procedure for a smooth function given on synthetic random data points.*

N $[10^3]$	*Mem* [MB]	*rat.* [%]	compr. t. [s]	GMRES #	sol. t. [s]
1	2.5	33.80	<1	25	<1
5	28.1	14.73	3	27	1
10	69.2	9.07	6	29	4
25	199.5	4.18	22	30	12
50	466.4	2.44	55	33	33
100	1122.4	1.47	141	40	110
500	7540.8	0.39	1028	199	3693

compression rate ("*rat.*") for the approximation as a measure of the data reduction achieved through ACA. The number of GMRES iterations (#) and CPU time ("sol. t.") are also given. We observe the almost linear storage and computation time increase. Similar results are obtained on measurement data sets depicted on Figures 4, 5, 6. The performance of the interpolation procedure is summarized in Table 2. After the system (5) has been solved, the interpolant (4) needs to be evaluated on a set of points $X' = \{y_j\}_{j=1}^{M}$,

$$s(y_j) = \sum_{i=1}^{N} a_i \phi(|x_i - y_j|) + P(y_j), \quad j = 1, ..., M.$$

Evaluation with a desired accuracy ε' can be accomplished efficiently by constructing the blockwise low-rank approximant to the rectangular $N \times M$ matrix filled with

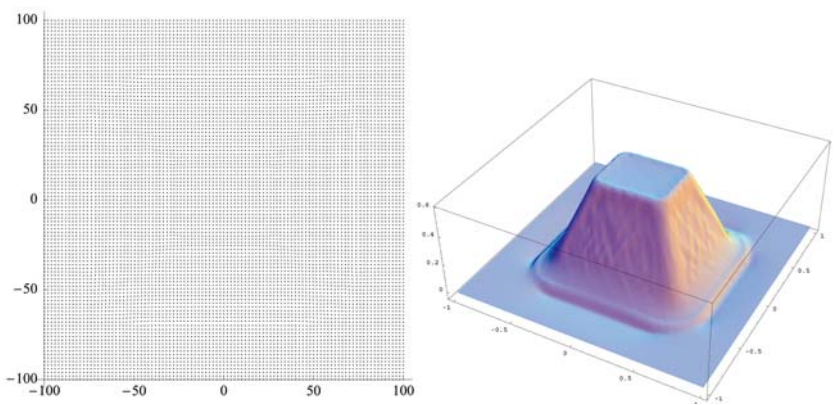

Fig. 4. Data set A and the corresponding interpolation results.

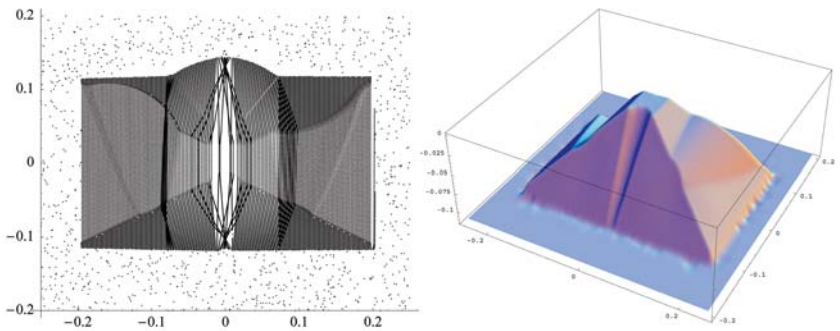

Fig. 5. Data set B and the corresponding interpolation results.

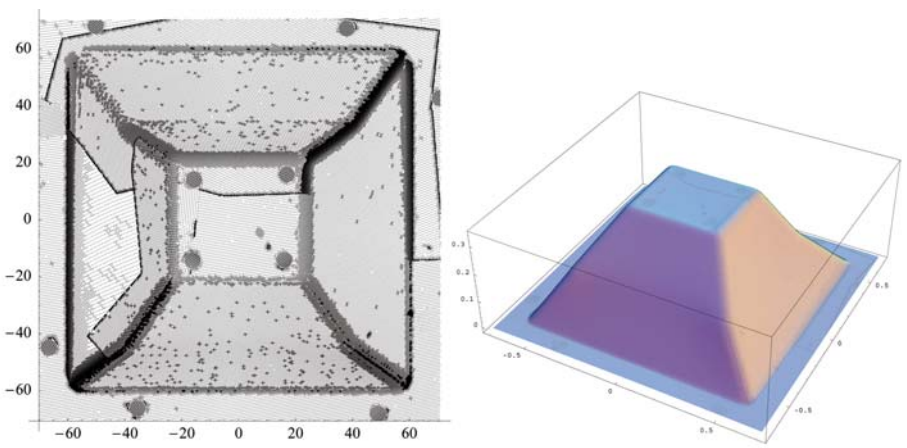

Fig. 6. Data set C and the corresponding interpolation results.

Table 2. *Performance of the interpolation procedure for data sets A, B and C.*

set	N	h_X	H_X	*rat.* [%]	compr. t. [s]	GMRES #	sol. t. [s]
A	10 201	6.0E-03	7.2e-03	8.40	10	36	6
B	30 727	4.3E-05	2.7e-02	3.97	25	118	64
C	118 205	2.9E-04	3.9e-03	1.35	220	141	413

entries $\phi(|x_i - y_j|)$, $i = 1, \ldots N$, $j = 1, \ldots, M$. Now the value of the ACA approximation accuracy ε can be chosen so that $\varepsilon \leq \varepsilon'$. With the coefficients a_i at hand, we can also find partial derivatives $s_1'(x)$ and $s_2'(x)$ of the interpolant. The evaluation of partial derivatives on X' is accomplished efficiently using the same blockwise low-

rank approximation strategy. In the case of s_1', we rewrite the derivative as

$$\begin{aligned} s_1'(y_j) &= \sum_{i=1}^{N} a_i \phi'_{y_{j,1}}(|x_i - y_j|) + c_1 \\ &= \sum_{i=1}^{N} a_i (2\log|x_i - y_j| + 1)(x_{i,1} - y_{j,1}) + c_1 \\ &= \tilde{\Phi}^1 a + c_1, \end{aligned}$$

where $x_i = (x_{i,1}, x_{i,2})$

$$\tilde{\Phi}^1_{ij} = \begin{cases} (2\log|x_i - y_j| + 1)(x_{i,1} - y_{j,1}) & \text{for } |x_i - y_j| > 0, \\ 0 & \text{otherwise.} \end{cases}$$

This generating function is asymptotically smooth. Therefore, the matrix $\tilde{\Phi}^1$ can be approximated by a blockwise low-rank using the ACA. The same argument holds for s_2' and the corresponding matrix $\tilde{\Phi}^2$.

Data sets for the interpolation are shown on Figures 4, 5 and 6 together with the corresponding interpolants. The performance of the ACA accelerated TPS interpolation procedure is summarised in Table 2.

In our application values of the partial derivatives are useful for computing the normal to the graph of s, which is necessary to estimate the thickness of the part. The

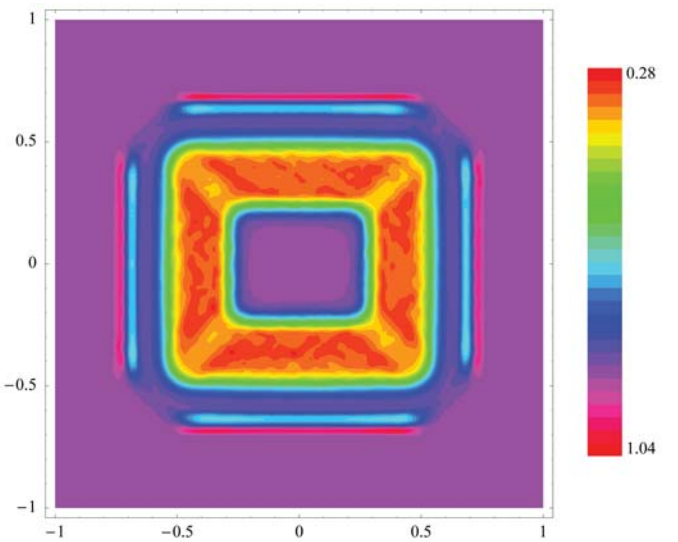

Fig. 7. Estimated distribution of thickness in mm along the deformed metal sheet.

computed thickness distribution for the data set A is shown in Figure 7. The initial thickness of the undeformed sheet is 1 mm. Comparing this distribution with the shape of the metal part, we see that the sheet appears thinner in areas where the slope is steep. Some small thickening regions along the sides of the deformed area are also observed. Overall, the developed interpolation technique can be used to calculate the thickness distribution of a sheet metal part non-destructively, provided that both sides can be accessed by a digitiser.

Although our study focuses on two-dimensional considerations, the method of constructing blockwise low-rank approximants to the corresponding matrices also applies to RBF interpolation in three or more dimensions.

4 - Fast Galerkin BEM for the Lamé system

Consider an elastic body $\Omega \subset \mathbb{R}^3$ with a Lipschitz boundary Γ. Suppose that a displacement of the body $\underline{g_D}$ is given on $\Gamma_D \subset \Gamma$ and some force $\underline{g_N}$ is applied to $\Gamma_N \subset \Gamma$. We also require that $\Gamma = \overline{\Gamma}_D \cup \overline{\Gamma}_N$. The displacement field $\underline{u} : \Omega \to \mathbb{R}^3$ satisfies the Lamé system of equations, therefore

$$\left\{ \begin{array}{rcll} \operatorname{div} \sigma(\underline{u}, x) & = & \underline{0}\,, & \text{for } x \in \Omega\,, \\ (\gamma_0 \underline{u})(x) & = & \underline{g_D}(x)\,, & \text{for } x \in \Gamma_D\,, \\ (\gamma_1 \underline{u})(x) & = & \underline{g_N}(x)\,, & \text{for } x \in \Gamma_N\,. \end{array} \right. \tag{7}$$

Here the divergence of stress $\sigma(\underline{u}, x)$ relates to partial derivatives of the displacement field $\underline{u}(x)$ and the material properties λ, μ

$$\operatorname{div} \sigma(\underline{u}, x) = \mu \, \Delta \underline{u}(x) + (\lambda + \mu) \operatorname{grad} \operatorname{div} \underline{u}(x)\,.$$

Lamé constants λ and μ are functions of elasticity modulus E and Poisson ratio ν of the material

$$\lambda = \frac{E\nu}{(1+\nu)(1-2\nu)}, \quad \mu = \frac{E}{2(1+\nu)}.$$

Dirichlet and Neumann trace operators are defined as

$$\begin{aligned} (\gamma_0 \underline{u})(x) &= \lim_{y \to x} \underline{u}(y)\,, \quad \text{for } y \in \Omega\,,\ x \in \Gamma\,, \\ (\gamma_1 \underline{u})(x) &= (\gamma_0 \sigma(\underline{u}, \cdot))(x)\, \underline{n}(x)\,, \end{aligned}$$

where $\underline{n}(x)$ denotes the outer unit normal of Γ.

The problem (7) admits the following symmetric boundary integral formulation (for details we refer to Sirtori [**23**] and Steinbach [**21**]):

$$
\begin{aligned}
(V\underline{t})(x) - (K\underline{g})(x) &= \left(\frac{1}{2}I + K\right)\underline{\tilde{g}_D}(x) - (V\underline{\tilde{g}_N})(x) \quad \text{for } x \in \Gamma_D,\\
(K'\underline{t})(x) + (D\underline{g})(x) &= \left(\frac{1}{2}I - K'\right)\underline{\tilde{g}_N}(x) - (D\underline{\tilde{g}_D})(x) \quad \text{for } x \in \Gamma_N,
\end{aligned}
\tag{8}
$$

where $\underline{g} = (\gamma_0\underline{u}) - \underline{\tilde{g}_D}$, $\underline{t} = (\gamma_1\underline{u}) - \underline{\tilde{g}_N}$, $\underline{\tilde{g}_N}$ and $\underline{\tilde{g}_D}$ are extensions of $\underline{g_N}$ and $\underline{g_D}$ to the whole boundary Γ. The following boundary integral operators are involved in (8)

$$
\begin{aligned}
(V\,\underline{w})(x) &= \gamma_0 \int_\Gamma U^*(x,y)\underline{w}(y)\,ds_y\,,\\
(K\,\underline{v})(x) &= \frac{1}{2}\underline{v}(x) + \gamma_0 \int_\Gamma \gamma_{1,y}U^*(x,y)\underline{v}(y)\,ds_y\,,\\
(K'\,\underline{w})(x) &= -\frac{1}{2}\underline{w}(x) + \gamma_1 \int_\Gamma U^*(x,y)\underline{w}(y)\,ds_y\,,\\
(D\,\underline{v})(x) &= -\gamma_1 \int_\Gamma \gamma_{1,y}U^*(x,y)\underline{v}(y)\,ds_y\,,
\end{aligned}
$$

are the single layer, double layer, adjoint double layer potentials, and a hyper-singular operator respectively. Here

$$
U^*_{k\ell}(x,y) = \frac{1+\nu}{8\pi E(1-\nu)}\left[(3-4\nu)\frac{\delta_{k\ell}}{|x-y|} + \frac{(x_k-y_k)(x_\ell-y_\ell)}{|x-y|^3}\right]
\tag{9}
$$

is the fundamental solution. For the mapping properties of the above operators we refer to [**21**]. In the special case when the displacements are prescribed on the whole boundary (i.e. $\Gamma_D = \Gamma$), the traction forces $\underline{t}$ can be computed from the first equation of (8)

$$
\underline{t}(x) = (S\,\underline{g_D})(x)\,,\quad x \in \Gamma\,.
\tag{10}
$$

Here S is the Steklov-Poincaré operator

$$
S = V^{-1}\Big(\frac{1}{2}I + K\Big).
\tag{11}
$$

It can also be written in a symmetric form as

$$
S = D + \Big(\frac{1}{2}I + K'\Big)V^{-1}\Big(\frac{1}{2}I + K\Big).
\tag{12}
$$

As soon as the complete Cauchy data is obtained as a solution of (8) (or by (10)), the displacements $\underline{u}(x)$ inside Ω can be computed as

$$\underline{u}(x) = \int_\Gamma U^*(x,y)\underline{t}(y)\,ds_y - \int_\Gamma \gamma_{1,y}U^*(x,y)\underline{g}(y)\,ds_y \quad \text{for } x \in \Omega\,.$$

To obtain a boundary element discretisation of the problem, we approximate Γ by a conform surface triangulation with N triangles and M nodes. We use the piecewise constant functions ($\psi_\ell(x)$ is 1 on triangle τ_ℓ and 0 outside τ_ℓ) as basis and test functions for the discretised single layer potentials. These functions also serve as test functions for the double layer potentials.

The basis functions for the hypersingular and the adjoint double layer potentials are chosen to be piecewise linear: $\varphi_j(x_i) = \delta_{ij}$, $\varphi_j(x)$ is linear on each τ_ℓ. These functions are also used as trial functions for hypersingular operators and double layer potentials. The Galerkin discretisation of (8) leads to the system

$$\begin{pmatrix} V_h & -K_h \\ K_h^T & D_h \end{pmatrix} \begin{pmatrix} t_h \\ g_h \end{pmatrix} = \begin{pmatrix} -V_h & \frac{1}{2}M_h + K_h \\ \frac{1}{2}M_h - K_h^T & -D_h \end{pmatrix} \begin{pmatrix} \tilde{g}_N \\ \tilde{g}_D \end{pmatrix} =: \begin{pmatrix} f_N \\ f_D \end{pmatrix}.$$

The above fully populated matrices are composed of the following three by three blocks

$$(V_h)_{k\ell} = \langle V(\psi_\ell \mathbf{i}), \psi_k \rangle, \quad (K_h)_{kj} = \langle K(\varphi_j \mathbf{i}), \psi_k \rangle, \quad (D_h)_{ij} = \langle D(\varphi_j \mathbf{i}), \varphi_i \rangle,$$

where $\mathbf{i}$ is a three by three identity matrix, $\langle \cdot, \cdot \rangle$ denotes the scalar product on $L^2(\Gamma)$, and $k, \ell = 1 \ldots N$, $i, j = 1 \ldots M$. The sparse mass matrix M_h consists of blocks

$$(M_h)_{kj} = \mathbf{i} \int_{\tau_k} \varphi_j(x) ds_x.$$

We renumber the degrees of freedom according to Cartesian directions. Thus, instead of composing the matrix V_h as N by N table of symmetric 3 by 3 blocks, we compose 6 symmetric N by N blocks. In these settings, elements of these large blocks have form (1). Because the integral kernels $U^*_{k\ell}$ are asymptotically smooth (i.e. satisfy (2)), the entire matrix V_h can be approximated by a blockwise low-rank hierarchical matrix. This approximant is efficiently obtained by means of the ACA.

To avoid computing entries of K_h and D_h, actions of operators K, K' and D are expressed through actions of the single and double layer potential operators for the Laplace equation V_L and K_L and certain tangential differential operators (see [**16**] and also [**21**]). Thus, the matrix-vector products $K_h v$, $K'_h v$ and $D_h v$ are ob-

tained by repeated applications of $V_{L,h}$, $K_{L,h}$ and some sparse matrices. As a result, the BEM for (8) is implemented with just eight blockwise low-rank matrices. They approximate $V_{L,h}$, $K_{L,h}$, and the six symmetric matrices corresponding to the second term in (9).

4.1 - *Effective elastic moduli of composite materials*

Many composite materials can be described as hard inclusions (e.g. particles of fibers) in a relatively soft medium (see Figure 8). Even if these inclusions constitute a small volume fraction, the effective mechanical properties of such material differ significantly from those of the pure soft medium. It is common to denote the inclusions by the term 'phase' and to refer to the medium by the term 'matrix'. Suppose that both the phase and the matrix materials are homogeneous and isotropic, then the composite may still exhibit strongly anisotropic behavior. In the range of linear deformations this anisotropy is completely described by 21 effective elastic moduli. One way to estimate these moduli is to perform a series of six numerical experiments, in which a representative volume element (RVE) is subjected to certain Dirichlet boundary conditions, and its reaction in a form of traction forces is obtained. Thus, the mathematical formulation of the problem consists of solving the Dirichlet boundary value problem of linear elastostatics in a domain with piecewise constant, isotropic material properties (see Fig. 8)

$$
(13)\qquad \begin{cases} -\mu_\alpha \Delta \underline{u}(x) - (\lambda_\alpha + \mu_\alpha)\,\mathrm{grad}\,\mathrm{div}\,\underline{u}(x) = \underline{0}\,, & x \in \Omega_\alpha,\ 0 \le \alpha \le N_{inc}, \\ (\gamma_0^0 \underline{u})(x) = \underline{g_R}(x)\,, & x \in \Gamma_R, \\ (\gamma_0^0 \underline{u})(x) = (\gamma_0^k \underline{u})(x)\,, & x \in \Gamma_k\,,\ 1 \le k \le N_{inc}, \\ (\gamma_1^0 \underline{u})(x) = -(\gamma_1^k \underline{u})(x)\,, & x \in \Gamma_k,\ 1 \le k \le N_{inc}\,, \end{cases}
$$

where Γ_R is the boundary of the RVE, and $\underline{g_R} : \Gamma_R \to \mathbb{R}^3$ is given. Dirichlet and

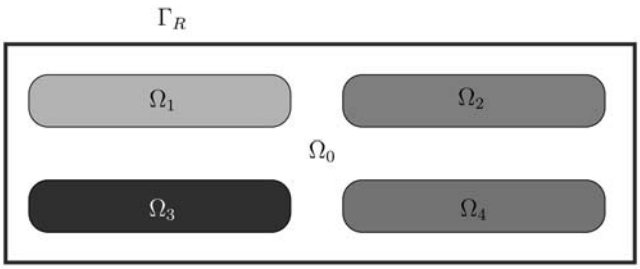

Fig. 8. Computational domain Ω with $N_{inc} = 4$ inclusions.

Neumann trace operators are defined for each Ω_α, $\alpha = 0, \ldots, N_{inc}$

$$(\gamma_0^\alpha \underline{u})(x) = \lim_{y \to x} \underline{u}(y), \quad \text{for } y \in \Omega_\alpha, \ x \in \Gamma_\alpha,$$

$$(\gamma_1^\alpha \underline{u})(x) = (\gamma_0^\alpha \sigma(\underline{u}, \cdot))(x)\, \underline{n_\alpha}(x),$$

where $\underline{n_\alpha}(x)$ denotes the outer unit normal of Γ_α. We denote the Cauchy data for the matrix domain Ω_0 by $\underline{g_0}$ and $\underline{t_0}$ and introduce the globally defined local Cauchy data for $x \in \Gamma_0$ and $k = 1, ..., N_{inc}$

$$\underline{g_k}(x) = \begin{cases} (\gamma_0^k \underline{u})(x), & \text{for } x \in \Gamma_k, \\ 0, & \text{for } x \in \Gamma_0 \setminus \Gamma_k, \end{cases}$$

$$\underline{t_k}(x) = \begin{cases} (\gamma_1^k \underline{u})(x), & \text{for } x \in \Gamma_k, \\ 0, & \text{for } x \in \Gamma_0 \setminus \Gamma_k. \end{cases}$$

We also extend the given Dirichlet datum $\underline{g_R}$ on Γ_R by zero to the whole boundary Γ_0. The continuity of the displacement field (the third condition in (13)) enables us to express the displacement $\underline{g_0}$ on the whole boundary a sum

$$\underline{g_0}(x) = \underline{g_R}(x) + \sum_{j=1}^{N_{inc}} \underline{g_j}(x) \quad \text{for } x \in \Gamma_0.$$

The equilibrium of forces on boundaries of inclusions (the fourth condition in (13)) yields the system for the unknown displacements $\underline{g_k}, k = 1, \ldots, N_{inc}$

$$\sum_{j=1}^{N_{inc}} \left(S_0 \underline{g_j}\right)(x) + \left(S_k \underline{g_k}\right)(x) = -\left(S_0 \underline{g_R}\right)(x), \quad \text{for } x \in \Gamma_k. \tag{14}$$

The Steklov-Poincaré operators S_α are selfadjoint and, in general, positive semi-definite. However, the Dirichlet boundary condition in (13) ensures that an appropriate Galerkin discretisation of the boundary integral equation (14) with (12) leads to a symmetric, positive definite system of linear equations. ACA accelerated Galerkin BEM was implemented for both symmetric (12) and non-symmetric (11) forms of the Steklov-Poincaré operator. The efficiency of the resulting solver can be demonstrated on the following example.

EXAMPLE 1. Consider a cube shaped RVE of a two component composite material depicted in Figure 9. The phase material with $E_i = 7.2 \cdot 10^4$ and $\nu_i = 0.4$ occupies the three balls, and the rest of the cube (about 90% of the volume) is filled with the matrix material with $E_0 = 1.9 \cdot 10^3$ and $\nu_0 = 0.3$. The entire boundary was discretised by the use of 4218 triangles. Distribution of magnitude

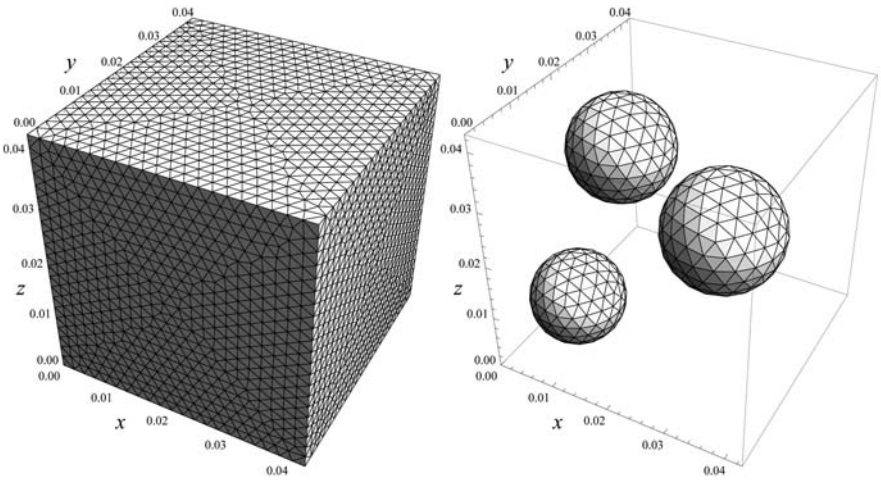

Fig. 9. Computational domain Ω with $N_{inc} = 3$ inclusions. Discretisations of Γ_R (left) and Γ_{inc} (right).

of tractions along the boundary of inclusions for one of the numerical experiments is depicted on Figure 10. We have also plotted the distribution of this quantity over the part of Γ_R, where $\mathrm{x} = 0$ (here $x = (\mathrm{x}, \mathrm{y}, \mathrm{z})^\top$). The resulting effective elasticity tensor of the equivalent homogeneous medium is dominated by its isotropic component (more than 90% of the tensor norm). The corresponding effective Young modulus and Poisson ratio are $\tilde{E} = 2399.9$ and $\tilde{\nu} = 0.288$. To demonstrate that the numerical complexity of the proposed solution method is almost linear, we perform the computations on a series of

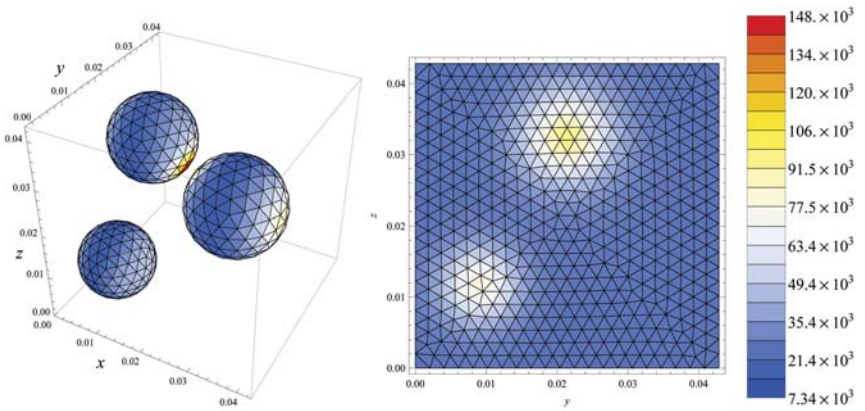

Fig. 10. Example 1. Distribution of the traction modulus $|\gamma_1^0 \underline{u}|$ along Γ_{inc} (left), and along the part of Γ_R, where $\mathrm{x} = 0$ (right).

Table 3. *Efficiency of the Galerkin BEM procedure. The ACA accuracy value is* $\varepsilon = 10^{-4}$ *for all experiments.*

ref.	elem.	mem. (MB)	compr. (%)	gen. t. (s)	sol. t. (s)	iter.	$\tilde{E}$	$\tilde{\nu}$
1	1092	36.7	52.68	116	32	138	2346.2	0.290
2	1994	97.5	42.10	257	85	120	2374.4	0.289
3	4218	270.5	26.18	580	221	145	2399.9	0.288
4	8204	634.4	16.22	1161	700	188	2413.4	0.288
2×8	10 036	886.1	15.28	1867	1181	235	2337.1	0.291
3×8	19 932	2123.4	9.29	4036	3597	290	2362.2	0.291

meshes. The efficiency results are summarised in Table 3. The number of degrees of freedom nearly doubles from one mesh to the next. The amount of memory required to store the H-matrices (column 3) and the matrix generation time (column 5) grow in a similar manner. This effect is due to increasing compression (column 4), and it expresses the almost linear complexity of the H-matrix/ACA procedure. We also observe, that the effective Young modulus $\tilde{E}$ (column 8) converges to its exact value from below. This should be viewed in contrast to FEM approach, when choosing linear elements introduces an artificial stiffness to the domain. In column 7, the number of GMRES iterations when solving the system in its non-symmetric form with relative tolerance 10^{-7} is shown. During the iterative solution procedure the Jacobi preconditioner was used. The last two lines of the Table 3 summarise the results of computations, where the RVE was taken to consist of eight copies of the one considered in Example 1. The difference in values of $\tilde{E}$ is now due to the fact, that the larger volume element is a better representation of the heterogeneous material (which has a periodic microstructure).

EXAMPLE 2. Consider a rectangular RVE of a two component composite material depicted on Figure 11. Fiber shaped inclusions consist of phase material with $E_i = 7.2 \cdot 10^4$ and $\nu_i = 0.23$. The rest of the RVE (about 85% of the volume) is filled with the matrix material with $E_{mat} = 1.9 \cdot 10^3$ and $\nu_{mat} = 0.44$. The entire boundary was discretised by the use of 26416 triangles. Distribution of magnitude of tractions along the deformed boundary of inclusions for a numerical experiment experiment (stretching in x direction) is depicted on Figure 12. We have also plotted the distribution of this quantity over the part of Γ_R, where $\mathrm{x} = \mathrm{x}_{min} = -7$. The resulting effective elastic moduli are

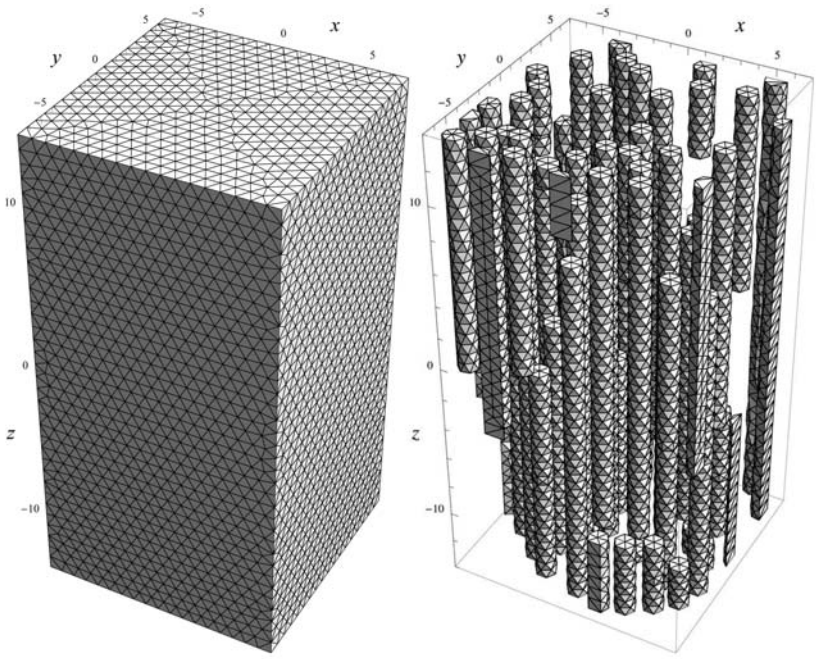

Fig. 11. Computational domain Ω with $N_{inc} = 65$ inclusions. Discretisations of Γ_R (left) and Γ_{inc} (left).

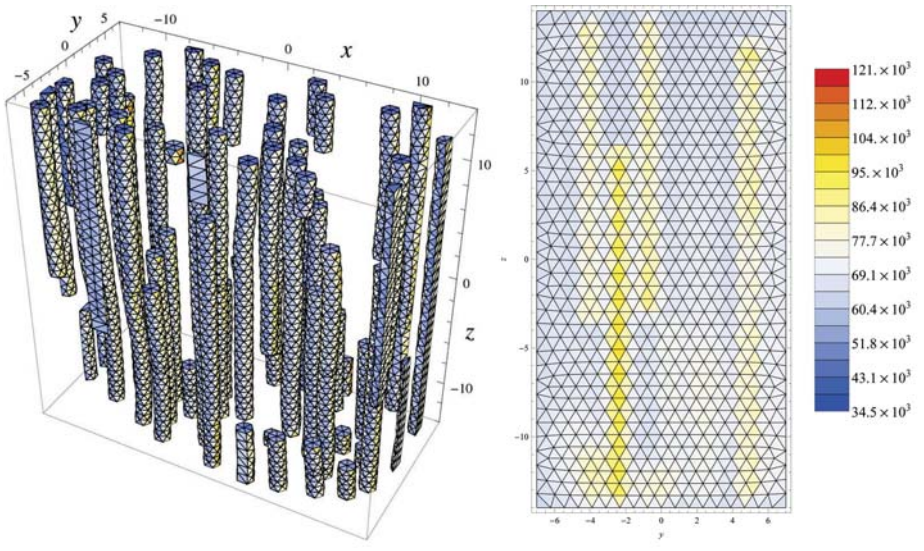

Fig. 12. Example 2. Distribution of the traction modulus $|\gamma_1^0 \underline{u}|$ along deformed Γ_{inc} (left), and along the part of Γ_R, where $\mathrm{x} = \mathrm{x}_{min}$ (right).

$$\tilde{C} = \begin{pmatrix} 7337.5 & 5556.6 & 5319.2 & 0.1 & -1.1 & -0.4 \\ & 7323.9 & 5317.3 & 0.1 & 0.4 & -5.6 \\ & & \mathbf{13\,202.0} & -10.5 & -21.4 & 1.0 \\ & \text{sym} & & 900.6 & -1.9 & -0.1 \\ & & & & 906.5 & -0.1 \\ & & & & & 886.5 \end{pmatrix}.$$

In this example, the anisotropy is clearly observed. It expresses itself through the large entry $\tilde{C}_{33}$. The isotropic component of the effective elasticity tensor accounts just for about 80% of the total norm.

4.2 - *FEM/BEM coupling for plastic elastic deformations*

The main drawback of BEM when applied to modeling of deformations lies in its inability to handle complex nonlinear material behavior (i.e. nonlinear stress-strain relations). For most materials these nonlinearities appear only when stress values are high. Situations, where the regions of high stress are small in comparison to the whole body, suggest the domain decomposition: deformations in the small plastic zone are modelled by an appropriate non-linear boundary value problem, and an efficient solution of the linear problem is arranged in the remaining large portion of the domain. Continuity conditions are posed on the interface between the two subdomains. To realise this modeling approach, we couple the fast Galerkin BEM solver with widely popular Finite Element solvers. The results are demonstrated on two examples.

EXAMPLE 3. Consider a benchmark problem in computational plasticity [**24**]. A steel plate with a cylindrical central hole is subjected to surface load $P = 360 \cdot 10^6 N/m^2$ on its upper and lower edges (see Figure 13 (left)). Material of von-Mises type is considered with no hardening and yield stress $450 \cdot 10^6 N/m^2$, Young's modulus $E = 206.9 \cdot 10^9 N/m^2$ and Poisson's ratio $\nu = 0.29$. Because of symmetries only a quarter of the plate is modelled. The domain decomposition and the meshes are shown on Figure 13 (middle). We couple the fast Galerkin BEM with the Finite Element Analysis Program (FEAP) [**25**] by the use of interface relaxation. The coupled system converged to the relative residual 10^{-4} in 24 coupling iterations. Yielded FEM elements are marked on Figure 13 (middle) and the x component of the resulting displacement field is plotted on Figure 13 (right). The results are in a good agreement with the reference solutions [**24**]. For detailed description of the coupled FEM-BEM procedure as well as for estimates of the FEM subdomain see [**12**].

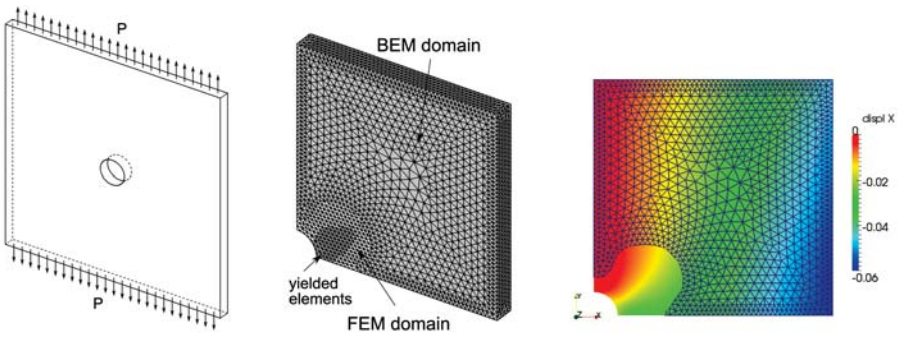

Fig. 13. Example 3. Domain and boundary conditions (left); subdomains, discretisation and yielded elements (middle); x-component of the displacement field (right).

EXAMPLE 4. An industrial application of the FEM-BEM coupling comes from modelling deep rolling process. Plastic deformations are induced along the surface of a turbine blade by means of rolling a spherical tool under pressure (see Figure 14 (left)). The rolled surface has increased tolerance to damage from eventual collisions with foreign objects. Experimental studies show, that in this process plastic deformations normally occur in a 0.5 mm thin boundary layer. The remaining part of the workpiece undergoes elastic deformations, which can alter the geometry of the blade. The coupled FEM-BEM solver was applied to the problem. The model geometry and the subdomains are depicted on Figure 14 (right). The tool-workpiece contact and the elastic-plastic modelling in the FEM subdomain was performed by the use of commercial software package ABAQUS, while the elastic deformations were handled by the fast Galerkin BEM solver. The continuity of displacement and stress fields on the interface was achieved by Dirichlet-Neumann iterations. The path of the tool was divided into a large number of increments (time steps), and the equilibrium of forces was computed after each such increment. Distributions of

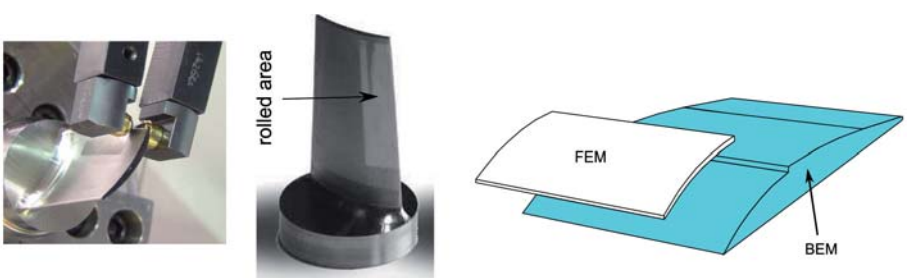

Fig. 14. Example 4. Deep rolling process (left), turbine blade with a rolled zone (middle); model geometry of FEM and BEM subdomains (right).

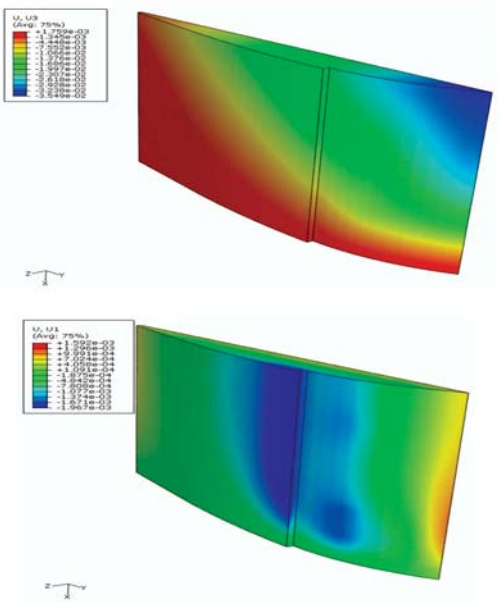

Fig. 15. Example 4. Distributions of z- and x-components of the displacement field along the boundary of BEM subdomain after the final rolling time step.

x- and z-components of the displacement field along the boundary of BEM subdomain after the final rolling time step are shown on Figure 15. The details of the implementation and comparison to pure FEM modeling of this process are described in [**2, 3**].

Acknowledgments. The authors acknowledge the collaboration of M. Bambach and V. Bäcker, RWTH Aachen, W. Elleithy, University of Linz as well as of H. Andrä and A. Zemitis, ITWM Kaiserslautern.

References

[1] H. Andrä, R. Grzhibovskis, S. Rjasanow and A. Zemitis, *Boundary element method for calculation of effective elastic moduli in 3D linear elasticity*, Math. Methods Appl. Sci. **33** (2010), 1021-1034.

[2] V. Bäcker, B. Feldhaus, R. Grzhibovskis, F. Klocke, S. Rjasanow and C. Zeppenfeld, *Coupled FE/BE-analysis of the deep rolling process*, In: D. Y. Yang, Y. H. Kim and C. H. Park, eds., *Advanced Technology of Plasticity*, Wiley-VCH Verlag, 2008, 299-300.

[3] V. Bäcker, F. Klocke, H. Wegner, A. Timmer, R. Grzhibovskis and S. Rjasanow, *Analysis of the deep rolling process on turbine blades using the FEM/BEM-coupling*, IOP Conference Series: Materials Science and Engineering, 10:012134, 2010.

[4] M. Bambach, R. Grzhibovskis, G. Hirt and S. Rjasanow, *Adaptive cross-approximation for surface reconstruction using radial basis functions*, J. Engrg. Math. **62** (2008), 149-160.

[5] I. Barrodale, R. Kuwahara, R. Poeckert and D. Skea, *Side-scan sonar image processing using thin plate splines and control point matching*, Numer. Algorithms **5** (1993), no. 1-4, 85-98.

[6] M. Bebendorf, *Approximation of boundary element matrices*, Numer. Math. **86** (2000), no. 4, 565-589.

[7] M. Bebendorf, *Hierarchical matrices. A means to efficiently solve elliptic boundary value problems*, Lecture Notes in Computational Science and Engineering (LNCSE), vol. 63, Springer-Verlag, Berlin 2008.

[8] M. Bebendorf and R. Grzhibovskis, *Accelerating Galerkin BEM for linear elasticity using adaptive cross approximation*, Math. Methods Appl. Sci. **29** (2006), no. 14, 1721-1747.

[9] M. Bebendorf and S. Rjasanow, *Adaptive low-rank approximation of collocation matrices*, Computing **70** (2003), 1-24.

[10] F. L. Bookstein, *Principal warps: Thin-plate splines and the decomposition of deformations*, IEEE Trans. Pattern Anal. Mach. Intell. **11** (1989), no. 6, 567-585.

[11] N. Dyn, D. Levin and S. Rippa, *Numerical procedures for surface fitting of scattered data by radial functions*, SIAM J. Sci. Statist. Comput. **7** (1986), no. 2, 639-659.

[12] W. Elleithy and R. Grzhibovskis, *An adaptive domain decomposition coupled finite element-boundary element method for solving problems in elasto-plasticity*, Internat. J. Numer. Methods Engrg. **79** (2009), no. 8, 1019-1040.

[13] J. Flusser, *An adaptive method for image registration*, Pattern Recognition **25** (1992), no. 1, 45-54.

[14] W. Hackbusch, *A sparse matrix arithmetic based on $\mathcal{H}$-matrices. I. Introduction to $\mathcal{H}$-matrices*, Computing **62** (1999), no. 2, 89-108.

[15] R. L. Hardy, *Theory and applications of the multiquadric-biharmonic method. 20 years of discovery 1968 -1988*, Comput. Math. Appl. **19** (1990), no. 8-9, 163-208.

[16] V. D. Kupradze, T. G. Gegelia, M. O. Basheleishvili and T. V. Burchuladze, *Three-dimensional problems of the mathematical theory of elasticity and thermoelasticity*, V. D. Kupradze, ed., North-Holland Ser. Appl. Math. Mech., vol. 25, North-Holland Pub. Co., Amsterdam-New York 1979.

[17] S. Kurz, O. Rain and S. Rjasanow, *The adaptive cross-approximation technique for the 3D boundary-element method*, IEEE Transaction on Magnetics **38** (2002), no. 2, 421-424.

[18] S. Kurz, O. Rain and S. Rjasanow, *Fast boundary element methods in computational electromagnetism*, In: M. Schanz and O. Steinbach, eds., *Boundary element analysis. Mathematical aspects and applications*, Springer, Berlin 2007, 249-279.

[19] C. A. MICCHELLI, *Interpolation of scattered data: distance matrices and conditionally positive definite functions*, Constr. Approx. **2** (1986), no. 1, 11-22.

[20] L. MIRSKY, *Symmetric gauge functions and unitarily invariant norms*, Quart. J. Math. Oxford Ser. (2) **11** (1960), 50-59.

[21] S. RJASANOW and O. STEINBACH, *The fast solution of boundary integral equations*, Mathematical and Analytical Techniques with Applications to Engineering, Springer, New York 2007.

[22] Y. SAAD and M. H. SCHULTZ, *GMRES: a generalized minimal residual algorithm for solving nonsymmetric linear systems*, SIAM J. Sci. Statist. Comput. **7** (1986), no. 3, 856-869.

[23] S. SIRTORI, G. MAIER, G. NOVATI and S. MICCOLI, *A Galerkin symmetric boundary-element method in elasticity: formulation and implementation*, Internat. J. Numer. Methods Engrg. **35** (1992), no. 2, 255-282.

[24] E. STEIN, P. WRIGGERS, A. RIEGER and M. SCHMIDT, *Benchmarks*, In: E. Stein, ed., *Error-controlled adaptive finite elements in solid mechanics*, Wiley, Chichester 2003, 385-404.

[25] R. L. TAYLOR, *FEAP – A finite element analysis program, Version 8.2, Theory Manual*, University of California at Berkeley, 2008.

RICHARDS GRZHIBOVSKIS
Universität des Saarlandes,
Fachrichtung 6.1 Mathematik
Postfach 151150
Saarbrücken, 66041, Germany
e-mail: richards@num.uni-sb.de

SERGEJ RJASANOW
Universität des Saarlandes,
Fachrichtung 6.1 Mathematik
Postfach 151150
Saarbrücken, 66041, Germany
e-mail: rjasanow@num.uni-sb.de